Journal of Systems Engineering and Electronics
Vol. PP, No. 99, May 2023, pp.1 – 14

Localization for mixed near-field and far-field sources under impulsive noise

GAO Hongyuan[1,*], ZHANG Yuze[1], DU Ya'nan[1], CHENG Jianhua[2], and CHEN Menghan[1]

1. College of Information and Communication Engineering, Harbin Engineering University, Harbin 150001, China;
2. College of Intelligent Systems Science and Engineering, Harbin Engineering University, Harbin 150001, China

Abstract: In order to solve the problem that the performance of traditional localization methods for mixed near-field sources (NFSs) and far-field sources (FFSs) degrades under impulsive noise, a robust and novel localization method is proposed. After eliminating the impacts of impulsive noise by the weighted outlier filter, the direction of arrivals (DOAs) of FFSs can be estimated by multiple signal classification (MUSIC) spectral peaks search. Based on the DOAs information of FFSs, the separation of mixed sources can be performed. Finally, the estimation of localizing parameters of NFSs can avoid two-dimension spectral peaks search by decomposing steering vectors. The Cramer-Rao bounds (CRB) for the unbiased estimations of DOA and range under impulsive noise have been drawn. Simulation experiments verify that the proposed method has advantages in probability of successful estimation (PSE) and root mean square error (RMSE) compared with existing localization methods. It can be concluded that the proposed method is effective and reliable in the environment with low generalized signal to noise ratio (GSNR), few snapshots, and strong impulse.

Keywords: source localization, far-field source (NFS), near-field source (FFS), impulsive noise, Cramer-Rao bound (CRB).

DOI: 10.23919/JSEE.2023.000065

1. Introduction

Since source localization is utilized broadly in radar, microphone array, and other fields, the research of localization methods has attracted the attention of many scholars [1]. Far-field source (FFS) can be regarded as plane wave when received by uniform linear array (ULA). For FFS, there is only one localizing parameter which is the direction of arrival (DOA) [2−4]. The subspace processing algorithms such as the multiple signal classification (MUSIC) algorithm [5,6] and the estimating signal parameters via rotational invariance techniques (ESPRIT) algorithm [7,8] are representative localization algorithms. However, near-field source (NFS) should be regarded as spherical wave. Both range and DOA need to be estimated [9−14]. The above-mentioned traditional localization methods are not suitable in the situation where FFSs and NFSs exist simultaneously.

Major localization methods for mixed sources can be divided into two categories. The first category of localization methods does not perform separation. For example, Liang et al. introduced high-order statistics (HOS) into the localization for mixed sources, and proposed a two-step MUSIC (TSMUSIC) algorithm [15]. The TSMUSIC algorithm extracted the DOAs information of both NFSs and FFSs to simplify the joint spectral peaks search. However, the construction of fourth-order statistics (FOS) led to excessive calculations. Jiang et al. proposed an efficient mixed sources localization algorithm based on the Root-MUSIC algorithm [16]. This method utilized root-finding calculation, which had smaller computational complexity compared to spectral peaks search. However, when the DOAs of FFSs and NFSs are similar, the performance of TSMUSIC and the algorithm in [16] deteriorates.

The second category of localization methods performs sources classification. He et al. proposed the MUSIC-based one-dimensional (1D) search (MBODS) algorithm which used oblique projection technology to realize the separation of mixed sources [17]. However, the performance can be affected by the array aperture loss. A mixed-order MUSIC (M-MUSIC) algorithm which used both FOS and second-order statistics (SOS) was proposed in [18]. This algorithm utilized MUSIC to obtain the DOAs of FFSs and constructed a special FOS matrix to realize the separation of the DOA and range. The second category has the problems of array aperture loss or HOS

Manuscript received March 23, 2022.
*Corresponding author.
This work was supported by the National Natural Science Foundation of China (62073093), the initiation fund for postdoctoral research in Heilongjiang Province (LBH-Q19098), and the Natural Science Foundation of Heilongjiang Province (LH2020F017).

which results in high computational complexity.

The above localization algorithms for mixed FFSs and NFSs are all designed under Gaussian background noise. However, in the actual environment, background noise is not an ideal Gaussian distribution. It is more reasonable to describe the background noise by symmetric alpha-stable (SαS) distribution with different characteristic exponent [19,20]. Because SαS distribution does not own SOS and HOS, traditional localization algorithms based on HOS and SOS are not suitable for impulsive noise. Fractional low-order covariance (FLOC) [21−23] and fractional low-order moment (FLOM) [24,25] were proposed for anti-impulsive noise interference. Qiu et al. proposed a search-free phased FLOM based generalized ESPRIT (SP-GESPRIT) method which introduced FLOC into the GESPRIT algorithm to achieve good performance under impulsive noise [13]. In scenarios where NFSs and FFSs coexist, it is difficult to combine existing FLOM and FLOC with HOS, which is widely used in the traditional localization methods for mixed sources.

In this paper, weighted outlier filter is introduced to the SOS-based algorithm to locate mixed sources under impulsive noise. The proposed method uses weighted outlier filter to deal with impulsive noise. Then the DOAs of FFSs can be estimated by the MUSIC algorithm. The orthogonality between steering vectors of different sources can be used to separate NFSs and FFSs. Finally, direction vectors which only contain DOAs information of NFSs can be used to perform DOAs estimation. Based on the DOA estimations of NFSs, the estimations of range are obtained through 1D spectral peaks search. The main contributions are as follows: (i) The weighted outlier filter is proposed to effectively suppress the impulsive noise. (ii) While ensuring the positioning accuracy, the proposed method relatively reduces the computational complexity, because there are no construction of extra matrices nor HOS while separating the DOA and range of NFS. (iii) The derivation of Cramer-Rao bounds (CRB) for mixed sources under SαS distribution background noise is proved.

This paper is organized as follows. The signal model and SαS distribution are described in Section 2. In Section 3, the proposed localization method for mixed sources under impulsive noise and the computational complexity are derived. In Section 4, the corresponding CRB is derived. In Section 5, simulation experiments are designed, and experimental conditions are given in detail. In Section 6, conclusions are drawn.

2. Signal model

There is a symmetric ULA which comprises $2L+1$ sensors with spacing d. There are B narrowband sources which are deterministic unknown sequence with zero means and wavelength λ imping on the ULA. Sources are statistically independent of each other. To avoid phase ambiguity, it is assumed that spacing $d \leqslant \lambda/4$ and the number of sensors meets $2L+1 > B$. The number of sources B can be used directly as prior knowledge by using the method in [26,27]. For analysis convenience, the 1th to B_1th sources are FFSs, and the (B_1+1)th to Bth sources are NFSs.

For the $t(t=1,2,\cdots,T)$th snapshot, the data received by the $l(l=-L,\cdots,0,\cdots,L)$th sensor has the following expression:

$$x_l(t)=\sum_{b=1}^{B} s_b(t)\mathrm{e}^{-\mathrm{j}w_0\tau_{l,b}}+n_l(t) \tag{1}$$

where $s_b(t)$ is the envelope function of the bth source, $n_l(t)$ is the impulsive noise received by the lth sensor, $\tau_{l,b}$ is the propagation delay of the bth source reaching the 0th and the lth sensor as shown in Fig. 1, and w_0 is the circular frequency of sources.

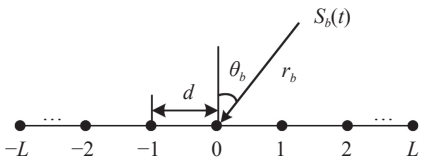

Fig. 1 ULA configuration

When the bth source is NFS, $-w_0\tau_{l,b}$ has the following expression:

$$-w_0\tau_{l,b}=2\pi r_b\left(\sqrt{1+\left(\frac{d_l}{r_b}\right)^2-2d_l\left(\frac{\sin\theta_b}{r_b}\right)}-1\right)\cdot\lambda^{-1} \tag{2}$$

where $d_l=ld$, θ_b is the DOA of the bth source, and r_b denotes the distance from the bth source to the 0th sensor. $-w_0\tau_{l,b}$ can be expanded through the Fresnel approximation:

$$-w_0\tau_{l,b}\approx\kappa_b l+\beta_b l^2 \tag{3}$$

where $\kappa_b=-2\pi\sin\theta_b d/\lambda$, $\beta_b=\pi\cos^2\theta_b d^2/(\lambda r_b)$.

When the bth source is FFS, $-w_0\tau_{l,b}$ can be simplified as

$$-w_0\tau_{l,b}=\kappa_b l. \tag{4}$$

$\boldsymbol{x}(t)$ is expressed in the following form:

$$\boldsymbol{x}(t)=\boldsymbol{A}_F\boldsymbol{s}_F(t)+\boldsymbol{A}_N\boldsymbol{s}_N(t)+\boldsymbol{n}(t), \tag{5}$$

where

$$\boldsymbol{x}(t)=[x_{-L}(t),x_{-L+1}(t),\cdots,x_L(t)]^{\mathrm{T}}\in\mathbf{C}^{(2L+1)\times 1}, \tag{6}$$

$$\boldsymbol{n}(t)=[n_{-L}(t),n_{-L+1}(t),\cdots,n_L(t)]^{\mathrm{T}}\in\mathbf{C}^{(2L+1)\times 1}, \tag{7}$$

$$\boldsymbol{s}_F(t)=[s_1(t),s_2(t),\cdots,s_{B_1}(t)]^{\mathrm{T}}\in\mathbf{C}^{B_1\times 1}, \tag{8}$$

$$\boldsymbol{A}_F=[\boldsymbol{a}(\theta_1),\boldsymbol{a}(\theta_2),\cdots,\boldsymbol{a}(\theta_{B_1})]\in\mathbf{C}^{(2L+1)\times B_1}, \tag{9}$$

$$\boldsymbol{a}(\theta_b)=[\mathrm{e}^{-\mathrm{j}L\kappa_b},\mathrm{e}^{-\mathrm{j}L\kappa_b+1},\cdots,\mathrm{e}^{\mathrm{j}L\kappa_b}]^{\mathrm{T}}, \tag{10}$$

$$\boldsymbol{s}_N(t)=[s_{B_1+1}(t),s_{B_1+2}(t),\cdots,s_B(t)]^{\mathrm{T}}\in\mathbf{C}^{(B-B_1)\times 1}, \tag{11}$$

$$\boldsymbol{A}_N=[\boldsymbol{a}(\theta_{B_1+1},r_{B_1+1}),\boldsymbol{a}(\theta_{B_2+1},r_{B_2+1})\cdots,\boldsymbol{a}(\theta_B,r_B)]\in\mathbf{C}^{(2L+1)\times(B-B_1)} \tag{12}$$

$$\boldsymbol{a}(\theta_b,r_b)=[\mathrm{e}^{\mathrm{j}(-L\kappa_b+L^2\beta_b)},\mathrm{e}^{\mathrm{j}(-L\kappa_b+L^2\beta_b+1)},\cdots,\mathrm{e}^{\mathrm{j}(L\kappa_b+L^2\beta_b)}]^{\mathrm{T}}. \tag{13}$$

$n_l(t)=\bar{n}_l(t)+j\tilde{n}_l(t)$ is the lth entry of $\boldsymbol{n}(t)$ and it is independent of the sources. $\bar{n}_l(t)$ and $\tilde{n}_l(t)$ represent the real and imaginary parts of $n_l(t)$, respectively. It is assumed that both $\bar{n}_l(t)$ and $\tilde{n}_l(t)$ follow the SαS distribution [28], so the characteristic function of $\bar{n}_l(t)$ and $\tilde{n}_l(t)$ can be expressed as

$$\varphi(u)=\exp\{\mathrm{j}\delta u-\gamma|u|^{\alpha}\} \tag{14}$$

where $\alpha(0<\alpha\leqslant 2)$ is the characteristic exponent, which determines the probability density function (PDF), $\delta(-\infty<\delta<\infty)$ is the location parameter which is the symmetry point of the PDF, and $\gamma(\gamma>0)$ is the dispersion parameter which indicates the width of distribution. With the increase of α, the tail of the PDF will become smaller. When $\alpha=2$, the SαS distribution degenerates to the Gaussian distribution. In this paper, background noise conforms to the standard SαS distribution($\delta=0$, $\gamma=1$).

3. Proposed algorithm

This section introduces the detailed principle of the proposed algorithm, and the computational complexity analysis of the proposed algorithm is also carried out.

3.1 Method of anti-impulsive noise

The absolute value of $x(t)$ can be expressed as $\tilde{\boldsymbol{x}}(t)=[\tilde{x}_{-L}(t),\tilde{x}_{-L+1}(t),\cdots,\tilde{x}_L(t)]^{\mathrm{T}}$. After taking $\boldsymbol{x}(t)$ as the input of filter with the length of window $2T_1+1$, the $(\bar{l},\bar{q})$th element $\boldsymbol{Z}(\bar{l},\bar{q})$ of the outlier matrix $\boldsymbol{Z}$ is given by

$$\boldsymbol{Z}(\bar{l},\bar{q})=p_3\mathrm{median}\left(\left|\tilde{x}_l(\bar{q})-\boldsymbol{m}(\bar{l},\bar{q})\right|,\left|\tilde{x}_l(\bar{q}+1)-\boldsymbol{m}(\bar{l},\bar{q}+1)\right|,\left|\tilde{x}_l(\bar{q}+2T_1)-\boldsymbol{m}(\bar{l},\bar{q})\right|\right) \tag{15}$$

where

$$\begin{cases}\bar{l}=l+L+1\\ \bar{q}=t-T_1\\ l=-L,\cdots,L\\ t=T_1+1,\cdots,2N+1-T_1\end{cases},$$

median(·) means taking the median value, $\boldsymbol{m}(\bar{l},\bar{q})=\mathrm{median}\tilde{x}_l(\bar{q}),(\tilde{x}_l(\bar{q}+1),\cdots,\tilde{x}_l(\bar{q}+2T_1))$, and p_3 is the threshold value. When $\left|\tilde{\boldsymbol{x}}_l(t)-\boldsymbol{m}(\bar{l},\bar{q})\right|\leqslant\boldsymbol{Z}(\bar{l},\bar{q})$, the lth entry of filtered data $\boldsymbol{y}(\bar{q})=[y_{-L}(\bar{q}),y_{-L+1}(\bar{q}),\cdots,y_L(\bar{q})]^{\mathrm{T}}$ can be expressed as

$$\boldsymbol{y}_l(\bar{q})=\boldsymbol{x}_l(t). \tag{16}$$

When $\left|\tilde{\boldsymbol{x}}_l(t)-\boldsymbol{m}(\bar{l},\bar{q})\right|>\boldsymbol{Z}(\bar{l},\bar{q})$,

$$\boldsymbol{y}_l(\bar{q})=\boldsymbol{m}^{p_1}(\bar{l},\bar{q})\boldsymbol{h}^{p_2}(\bar{l},\bar{q})\boldsymbol{x}_l(t)\cdot\tilde{\boldsymbol{x}}_l(t)^{-1} \tag{17}$$

where $\boldsymbol{h}(\bar{l},\bar{q})=\mathrm{mean}(\tilde{x}_l(\bar{q}),\ \tilde{x}_l(\bar{q}+1),\ \cdots,\ \tilde{x}_l(\bar{q}+2T_1))$, mean(·) represents the average of the elements which are less than the median value of ·, and p_1 and p_2 are weighting factors ($p_1<1$, $p_2<1$, $p_1+p_2=1$).

After being preprocessed by the weighted outlier filter, the impulsive noise component of the received data is smoothed.

3.2 DOA estimation of FFS

The covariance matrix $\boldsymbol{R}_y$ has the following expression:

$$\boldsymbol{R}_y=\mathrm{E}\left\{\boldsymbol{y}(\bar{q})\boldsymbol{y}^{\mathrm{H}}(\bar{q})\right\}=\boldsymbol{R}_F+\boldsymbol{R}_N+\sigma^2\boldsymbol{I} \tag{18}$$

where $\boldsymbol{R}_F$ represents the covariance matrix of FFSs, $\boldsymbol{R}_N$ represents the covariance matrix of NFSs, and σ^2 is the power of additive background noise preprocessed by the weighted outlier filter.

The eigen-decomposition of covariance matrix $\boldsymbol{R}_y$ is shown as

$$\boldsymbol{R}_y=\boldsymbol{U}_s\boldsymbol{V}_s\boldsymbol{U}_s^{\mathrm{H}}+\boldsymbol{U}_n\boldsymbol{V}_n\boldsymbol{U}_n^{\mathrm{H}}. \tag{19}$$

In (19), $\boldsymbol{U}_s\in\mathbf{C}^{(2L+1)\times B}$ is made of the B eigenvectors belonging to B larger eigenvalues; $\boldsymbol{U}_n\in\mathbf{C}^{(2L+1)\times(2L+1-B)}$ is made of the $2L+1-B$ eigenvectors belonging to remaining $2L+1-B$ smaller eigenvalues; diagonal matrix $\boldsymbol{V}_s$ consists of the B larger eigenvalues; diagonal matrix $\boldsymbol{V}_n$ is made of the remaining smaller $2L+1-B$ eigenvalues.

Since the range parameter of the FFS is ∞, the DOAs information of FFSs can be estimated from the following spectral function:

$$f_1(\theta)=\left|\boldsymbol{a}^{\mathrm{H}}(\theta)\boldsymbol{U}_n\boldsymbol{U}_n^{\mathrm{H}}\boldsymbol{a}(\theta)\right|^{-1}. \tag{20}$$

where $\theta\in[-90°,90°]$

3.3 Sources classification and parameter estimation of NFS

On the basis of the DOA estimations of FFSs $\tilde{\theta}_b(b=1,2,\cdots,B_1)$, the power of the bth source is obtained by

utilizing the orthogonality between the different steering vectors:

$$\sigma_b^2 = \left(\boldsymbol{a}^{\mathrm{H}}(\tilde{\theta}_b)\boldsymbol{R}^{\perp}\boldsymbol{a}(\tilde{\theta}_b)\right)^{-1} \tag{21}$$

where '$\perp$' denotes the pseudo inverse operator. $\tilde{\boldsymbol{R}}_F$ can be expressed as

$$\tilde{\boldsymbol{R}}_F = \tilde{\boldsymbol{A}}_F \mathrm{diag}(\sigma_1^2, \sigma_2^2, \cdots, \sigma_{B_1}^2)\tilde{\boldsymbol{A}}_F^{\mathrm{H}} \tag{22}$$

where $\tilde{\boldsymbol{A}}_F = \left[\boldsymbol{a}(\tilde{\theta}_1), \boldsymbol{a}(\tilde{\theta}_2), \cdots, \boldsymbol{a}(\tilde{\theta}_{B_1})\right]$. Then the estimation of $\boldsymbol{R}_N$ can be obtained by

$$\tilde{\boldsymbol{R}}_N = \boldsymbol{R}_y - \tilde{\boldsymbol{R}}_F. \tag{23}$$

It can be seen from (23) that $\tilde{\boldsymbol{R}}_N$ does not contain the information of FFSs. An effective classification method is realized. The eigen-decomposition of $\tilde{\boldsymbol{R}}_N$ is shown as

$$\tilde{\boldsymbol{R}}_N = \boldsymbol{U}_{N,s}\boldsymbol{V}_{N,s}\boldsymbol{U}_{N,s}^{\mathrm{H}} + \boldsymbol{U}_{N,n}\boldsymbol{V}_{N,n}\boldsymbol{U}_{N,n}^{\mathrm{H}} \tag{24}$$

In (24), $\boldsymbol{U}_{N,s} \in \mathbf{C}^{(2L+1)\times(B-B_1)}$ is made of the $B-B_1$ eigenvectors belonging to $B-B_1$ larger eigenvalues; $\boldsymbol{U}_{N,n} \in \mathbf{C}^{(2L+1)\times(2L+1-B+B_1)}$ is made of the $2L+1-B+B_1$ eigenvectors belonging to remaining $2L+1-B+B_1$ smaller eigenvalues; diagonal matrix $\boldsymbol{V}_{N,s}$ consists of the $B-B_1$ larger eigenvalues; diagonal matrix $\boldsymbol{V}_{N,n}$ is made of the remaining smaller $2L+1-B+B_1$ eigenvalues. The steering vector $\boldsymbol{a}(\theta_b, r_b)$ of NFS can be divided into a direction vector $\boldsymbol{g}(\theta_b)$ and an integrated vector $\boldsymbol{c}(\theta_b, r_b)$ as follows:

$$\boldsymbol{a}(\theta_b, r_b) = \boldsymbol{g}(\theta_b)\boldsymbol{c}(\theta_b, r_b) \tag{25}$$

where

$$\boldsymbol{g}(\theta_b) = \begin{bmatrix} \mathrm{e}^{\mathrm{j}L\kappa_b} & 0 & \cdots & 0 \\ 0 & \mathrm{e}^{\mathrm{j}(-L+1)\kappa_b} & \cdots & 0 \\ \vdots & \vdots & \ddots & \vdots \\ 0 & 0 & \cdots & 1 \\ \vdots & \vdots & \iddots & \vdots \\ 0 & \mathrm{e}^{\mathrm{j}(L-1)\kappa_b} & \cdots & 0 \\ \mathrm{e}^{\mathrm{j}L\kappa_b} & 0 & \cdots & 0 \end{bmatrix}, \tag{26}$$

$$\boldsymbol{c}(\theta_b, r_b) = \left[\mathrm{e}^{\mathrm{j}L^2\beta_b}, \mathrm{e}^{\mathrm{j}(L-1)^2\beta_b}, \cdots, 1\right]. \tag{27}$$

The spectral function can be expressed as

$$f_2(\theta, r) = \left|(\boldsymbol{g}(\theta)c(\theta, r))^{\mathrm{H}}\boldsymbol{U}_{N,n}\boldsymbol{U}_{N,n}^{\mathrm{H}}\boldsymbol{g}(\theta)\boldsymbol{c}(\theta, r)\right|^{-1}. \tag{28}$$

where $r \in \left[0.62(((2L+1)d)^3/\lambda)^{0.5}, 2((2L+1)d)^2/\lambda\right]$.

Only when the DOA of NFS takes the true value, $\boldsymbol{G}(\theta) = \boldsymbol{g}^{\mathrm{H}}(\theta)\boldsymbol{U}_{N,n}\boldsymbol{U}_{N,n}^{\mathrm{H}}\boldsymbol{g}(\theta)$ becomes a singular matrix, and $\det(G(\theta)) = 0$, where $\det(\cdot)$ represents the determinant. Function (28) can be simplified as

$$f_2(\theta) = \left(\det(\boldsymbol{g}^{\mathrm{H}}(\theta)\boldsymbol{U}_{N,n}\boldsymbol{U}_{N,n}^{\mathrm{H}}\boldsymbol{g}(\theta))\right)^{-1}. \tag{29}$$

By decomposing the steering vector, joint DOA and range spectral peaks search can be simplified to DOA spectral peaks search. Thus, DOAs information of NFSs can be obtained. Then the ranges estimation of NFS can be obtained by taking the DOAs estimation of NFSs $\tilde{\theta}_b (b = B_1+1, B_1+2, \cdots, B)$ into the following spectral function:

$$f_3(\tilde{\theta}_b, r) = \left|\boldsymbol{a}^{\mathrm{H}}(\tilde{\theta}_b, r)\boldsymbol{U}_n\boldsymbol{U}_n^{\mathrm{H}}\boldsymbol{a}(\tilde{\theta}_b, r)\right|^{-1}. \tag{30}$$

3.4 Computational complexity

When discussing the computational complexity of localization for mixed FFS and NFS, only the major computational complexity is considered such as cumulant matrix construction, eigen-decomposition, spectral search, and root-polynomial construction and solution. The major computational complexity of M-MUSIC method includes construction of two $(2L+1)\times(2L+1)$-dimensional matrices, eigen-decomposition of above two matrices, implementation 1D spectral search for three times, the computational complexity of M-MUSIC is

$$O(9(2L+1)^2T + (2L+1)^2T + 8(2L+1)^3/3 + 2(2L+1)^2 180/\Delta_\theta + (B-B_1)(2L+1)^2 \cdot (2(2Ld)^2/\lambda - 0.62((2Ld)^3/\lambda)^{\frac{1}{2}}) \cdot \Delta_r^{-1})$$

where Δ_θ and Δ_r are search intervals, DOA search range is $[-90^\circ, 90^\circ]$. The range of NFS can only be in $[0.62((2Ld)^3/\lambda)^{1/2}, 2(2Ld)^2/\lambda]$. The major computational complexity of the MBODS method can be expressed as

$$O(2(2L+1)^2T + L_1(2L+2-L_1)^2 + 4(2L+1)^3/3 + 4(2L+2-L_1)^3/3 + 180(2L+1)^2/\Delta_\theta + 180(2L+2-L_1)^2/\Delta_\theta + (B-B_1)(2L+1)^2(2(2Ld)^2/\lambda - 0.62((2Ld)^3/\lambda)^{1/2})/\Delta_r)$$

where L_1 is the number of sub-arrays. The major computational complexity of the SP-GESPRIT method in [13] is

$$O((2L+1)^2T + 4(2L+1)^3/3 + 2BL + B^2(2L+1)).$$

The computational complexity of the proposed method is

$$O((2L+1)^2T + 8(2L+1)^3/3 + 2(2L+1)^2 180/\Delta_\theta + (B-B_1)(2L+1)^2(2(2Ld)^2/\lambda - 0.62((2Ld)^3/\lambda)^{1/2})/\Delta_r).$$

From the above analysis, it can be concluded that the proposed method reduces the computational complexity relatively.

4. CRB

The variance of any unbiased estimator cannot be smaller than the CRB [13,17,28−30]. The CRB analysis in [17] assumed that sources consist of both FFSs and NFSs

under Gaussian noise. In the actual work environment, background noise is not an ideal Gaussian distribution. The derivation of CRB for the mixed sources under the background noise which follows SαS distribution will be proved in this section.

Under the signal model in Section 2, the estimated vector is

$$\boldsymbol{\xi} = \left[\boldsymbol{S}^{\mathrm{T}}, \boldsymbol{\theta}_F^{\mathrm{T}}, \boldsymbol{\theta}_N^{\mathrm{T}}, \boldsymbol{r}^{\mathrm{T}}\right]^{\mathrm{T}}$$

where

$$\begin{aligned}
\boldsymbol{\theta}_F^{\mathrm{T}} &= [\theta_1, \theta_2, \cdots, \theta_{B_1}], \\
\boldsymbol{\theta}_N^{\mathrm{T}} &= [\theta_{B_1+1}, \theta_{B_1+2}, \cdots, \theta_B], \\
\boldsymbol{r}^{\mathrm{T}} &= [r_{B_1+1}, r_{B_1+2}, \cdots, r_B], \\
\boldsymbol{S}^{\mathrm{T}} &= \big[\mathrm{Re}(\boldsymbol{s}^{\mathrm{T}}(1)), \mathrm{Im}(\boldsymbol{s}^{\mathrm{T}}(1)), \mathrm{Re}(\boldsymbol{s}^{\mathrm{T}}(2)), \mathrm{Im}(\boldsymbol{s}^{\mathrm{T}}(2)), \cdots, \\
&\quad \mathrm{Re}(\boldsymbol{s}^{\mathrm{T}}(T)), \mathrm{Im}(\boldsymbol{s}^{\mathrm{T}}(T))\big], \\
\boldsymbol{s}(t) &= [s_1(t), s_2(t), \cdots, s_B(t)]^{\mathrm{T}}.
\end{aligned}$$

The PDF of $n_l(t)$ can be expressed as $f_n(\bar{n}, \tilde{n})$, thus the PDF of received data is

$$\begin{aligned}
f(\boldsymbol{X}) = \prod_{t=1}^{T} \prod_{l=-L}^{L} f_n(&\mathrm{Re}(\boldsymbol{x}_l(t)) - \mathrm{Re}(\boldsymbol{A}_l \boldsymbol{s}(t)), \\
&\mathrm{Im}(\boldsymbol{x}_l(t)) - \mathrm{Im}(\boldsymbol{A}_l \boldsymbol{s}(t)))
\end{aligned} \tag{31}$$

where $\boldsymbol{A} = [\boldsymbol{A}_F, \boldsymbol{A}_N]$, $\boldsymbol{A}_l$ represents the lth row vector of matrix $\boldsymbol{A}$, $\boldsymbol{x}_l(t)$ is the lth element of $x(t)$, and $\boldsymbol{X} = [\boldsymbol{x}(1), \boldsymbol{x}(2), \cdots, \boldsymbol{x}(T)]$. Take the logarithm of $f(\boldsymbol{X})$:

$$\begin{aligned}
\ln f(\boldsymbol{X}) = \sum_{t=1}^{T} \sum_{l=-L}^{L} \ln f_n(&\mathrm{Re}(x_l(t)) - \mathrm{Re}(\boldsymbol{A}_l \boldsymbol{s}(t)), \\
&\mathrm{Im}(x_l(t)) - \mathrm{Im}(\boldsymbol{A}_l \boldsymbol{s}(t))).
\end{aligned} \tag{32}$$

The derivative of (32) with $\mathrm{Re}(\boldsymbol{s}(t))$, $\mathrm{Im}(\boldsymbol{s}(t))$, $\boldsymbol{\theta}_F$, $\boldsymbol{\theta}_N$, and $\boldsymbol{r}$ can be calculated respectively:

$$\begin{aligned}
&\frac{\partial \ln f(\boldsymbol{X})}{\partial \mathrm{Re}(\boldsymbol{s}(t))} = \\
&\sum_{l=-L}^{L} \left(-\frac{\partial \ln f_n(\bar{n}, \tilde{n})}{\partial \bar{n}} \mathrm{Re}(\boldsymbol{A}_l^{\mathrm{T}}) - \frac{\partial \ln f_n(\bar{n}, \tilde{n})}{\partial \tilde{n}} \mathrm{Im}(\boldsymbol{A}_l^{\mathrm{T}}) \right),
\end{aligned} \tag{33}$$

$$\begin{aligned}
&\frac{\partial \ln f(\boldsymbol{X})}{\partial \mathrm{Im}(\boldsymbol{s}(t))} = \\
&\sum_{l=-L}^{L} \left(\frac{\partial \ln f_n(\bar{n}, \tilde{n})}{\partial \bar{n}} \mathrm{Im}(\boldsymbol{A}_l^{\mathrm{T}}) - \frac{\partial \ln f_n(\bar{n}, \tilde{n})}{\partial \tilde{n}} \mathrm{Re}(\boldsymbol{A}_l^{\mathrm{T}}) \right),
\end{aligned} \tag{34}$$

$$\begin{aligned}
\frac{\partial \ln f(\boldsymbol{X})}{\partial \boldsymbol{\theta}_F} = \sum_{t=1}^{T} \sum_{l=-L}^{L} \Bigg(&-\frac{\partial \ln f_n(\bar{n}, \tilde{n}))}{\partial \bar{n}} \mathrm{Re}(\boldsymbol{d}_{F,l} \boldsymbol{S}_F(t))^{\mathrm{T}} - \\
&\frac{\partial \ln f_n(\bar{n}, \tilde{n})}{\partial \tilde{n}} \mathrm{Im}(\boldsymbol{d}_{F,l} \boldsymbol{S}_F(t))^{\mathrm{T}} \Bigg),
\end{aligned} \tag{35}$$

$$\begin{aligned}
\frac{\partial \ln f(\boldsymbol{X})}{\partial \boldsymbol{\theta}_N} = \sum_{t=1}^{T} \sum_{l=-L}^{L} \Bigg(&-\frac{\partial \ln f_n(\bar{n}, \tilde{n})}{\partial \bar{n}} \mathrm{Re}(\boldsymbol{d}_{N,l} \boldsymbol{S}_N(t))^{\mathrm{T}} - \\
&\frac{\partial \ln f_n(\bar{n}, \tilde{n})}{\partial \tilde{n}} \mathrm{Im}(\boldsymbol{d}_{N,l} \boldsymbol{S}_N(t))^{\mathrm{T}} \Bigg),
\end{aligned} \tag{36}$$

$$\begin{aligned}
\frac{\partial \ln f(\boldsymbol{X})}{\partial \boldsymbol{r}} = \sum_{t=1}^{T} \sum_{l=-L}^{L} \Bigg(&-\frac{\partial \ln f_n(\bar{n}, \tilde{n})}{\partial \bar{n}} \mathrm{Re}(\boldsymbol{d}_{r,l} \boldsymbol{S}_N(t))^{\mathrm{T}} - \\
&\frac{\partial \ln f_n(\bar{n}, \tilde{n})}{\partial \tilde{n}} \mathrm{Im}(\boldsymbol{d}_{r,l} \boldsymbol{S}_N(t))^{\mathrm{T}} \Bigg)
\end{aligned} \tag{37}$$

where

$$\boldsymbol{d}_{F,l} = \left[\frac{\partial a_l(\theta_1)}{\partial \theta_1}, \frac{\partial a_l(\theta_2)}{\partial \theta_2}, \cdots, \frac{\partial a_l(\theta_{B_1})}{\partial \theta_{B_1}} \right], \tag{38}$$

$$\boldsymbol{d}_{N,l} = \left[\frac{\partial a_l(\theta_{B_1+1}, r_{B_1+1})}{\partial \theta_{B_1+1}}, \frac{\partial a_l(\theta_{B_1+2}, r_{B_1+2})}{\partial \theta_{B_1+2}}, \cdots, \frac{\partial a_l(\theta_B, r_B)}{\partial \theta_B} \right], \tag{39}$$

$$\boldsymbol{d}_{r,l} = \left[\frac{\partial a_l(\theta_{B_1+1}, r_{B_1+1})}{\partial r_{B_1+1}}, \frac{\partial a_l(\theta_{B_1+2}, r_{B_1+2})}{\partial r_{B_1+2}}, \cdots, \frac{\partial a_l(\theta_B, r_B)}{\partial r_B} \right], \tag{40}$$

$$\boldsymbol{S}_F(t) = \mathrm{diag}\{s_1(t), s_2(t), \cdots, s_{B_1}(t)\}, \tag{41}$$

$$\boldsymbol{S}_N(t) = \mathrm{diag}\{s_{B_1+1}(t), s_{B_1+2}(t), \cdots, s_B(t)\}. \tag{42}$$

According to the properties in [28], the PDF of $f_n(\bar{n}, \tilde{n})$ is circularly symmetric, $f_n(\pm\bar{n}, \pm\tilde{n}) = f_n(\bar{n}, \tilde{n}) = f_n(\sqrt{\tilde{n}^2 + \bar{n}^2})$, where $\bar{n}$ and $\tilde{n}$ are zero means and uncorrelated.

$$\begin{aligned}
I_c = \mathrm{E}\left\{ \left(\frac{\partial f_n(\bar{n}, \tilde{n})}{\partial \bar{n}} \right)^2 \right\} = \mathrm{E}\left\{ \left(\frac{\partial f_n(\bar{n}, \tilde{n})}{\partial \tilde{n}} \right)^2 \right\} = \\
\pi \int_0^{\infty} \frac{(f'_n(u))^2}{f_n(u)} u \mathrm{d}u.
\end{aligned} \tag{43}$$

The covariance matrix of sources is

$$\boldsymbol{Q} = \mathrm{E}\left\{ \boldsymbol{s}(t) \boldsymbol{s}^{\mathrm{H}}(t) \right\}. \tag{44}$$

Due to the signal sources consist of both FFSs and NFSs, $\boldsymbol{Q}$ can be divided into four parts:

$$\boldsymbol{Q} = \begin{bmatrix} \boldsymbol{Q}_1 & \boldsymbol{Q}_2 \\ \boldsymbol{Q}_3 & \boldsymbol{Q}_4 \end{bmatrix} \tag{45}$$

where $\boldsymbol{Q}_1 \in \mathbf{C}^{B_1 \times B_1}$, $\boldsymbol{Q}_2 \in \mathbf{C}^{B_1 \times (B-B_1)}$, $\boldsymbol{Q}_3 \in \mathbf{C}^{(B-B_1) \times B_1}$, and $\boldsymbol{Q}_4 \in \mathbf{C}^{(B-B_1) \times (B-B_1)}$. The Fisher information matrix is given by

$$\boldsymbol{J}(\boldsymbol{\xi}) = \mathrm{E}\left\{ \left(\frac{\partial \ln f(\boldsymbol{X})}{\partial \boldsymbol{\xi}} \right) \left(\frac{\partial \ln f(\boldsymbol{X})}{\partial \boldsymbol{\xi}} \right)^{\mathrm{T}} \right\}. \tag{46}$$

Similar to the operation presented in [13], the Fisher information matrix can be partitioned as

$$\boldsymbol{J}(\boldsymbol{\xi})=\begin{bmatrix} \overline{\boldsymbol{M}} & -\tilde{\boldsymbol{M}} & \cdots & 0 & 0 & \bar{\boldsymbol{\varepsilon}}(1) \\ \tilde{\boldsymbol{M}} & \overline{\boldsymbol{M}} & \cdots & 0 & 0 & \tilde{\boldsymbol{\varepsilon}}(1) \\ \vdots & \vdots & \ddots & & & \vdots \\ 0 & 0 & & \overline{\boldsymbol{M}} & -\tilde{\boldsymbol{M}} & \bar{\boldsymbol{\varepsilon}}(T) \\ 0 & 0 & & \tilde{\boldsymbol{M}} & \overline{\boldsymbol{M}} & \tilde{\boldsymbol{\varepsilon}}(T) \\ \bar{\boldsymbol{\varepsilon}}^{\mathrm{T}}(1) & \tilde{\boldsymbol{\varepsilon}}^{\mathrm{T}}(1) & \cdots & \bar{\boldsymbol{\varepsilon}}^{\mathrm{T}}(T) & \tilde{\boldsymbol{\varepsilon}}^{\mathrm{T}}(T) & \boldsymbol{\Gamma} \end{bmatrix} \tag{47}$$

where

$$\boldsymbol{M}=I_c\boldsymbol{A}^{\mathrm{H}}\boldsymbol{A}, \tag{48}$$

$$\boldsymbol{\varepsilon}(t)=I_c[\boldsymbol{A}^{\mathrm{H}}\boldsymbol{D}_F\boldsymbol{S}_F(t),\boldsymbol{A}^{\mathrm{H}}\boldsymbol{D}_N\boldsymbol{S}_N(t),\boldsymbol{A}^{\mathrm{H}}\boldsymbol{D}_r\boldsymbol{S}_N(t)], \tag{49}$$

$$\boldsymbol{\Gamma}=I_c\sum_{t=1}^{T}\mathrm{Re}\left\{\begin{bmatrix} \boldsymbol{S}_F^{H}(t)\boldsymbol{D}_F^{\mathrm{H}}\boldsymbol{D}_F\boldsymbol{S}_F(t), & \boldsymbol{S}_F^{\mathrm{H}}(t)\boldsymbol{D}_F^{\mathrm{H}}\boldsymbol{D}_N\boldsymbol{S}_N(t), & \boldsymbol{S}_F^{\mathrm{H}}(t)\boldsymbol{D}_F^{\mathrm{H}}\boldsymbol{D}_r\boldsymbol{S}_N(t) \\ \boldsymbol{S}_N^{\mathrm{H}}(t)\boldsymbol{D}_N^{\mathrm{H}}\boldsymbol{D}_F\boldsymbol{S}_F(t), & \boldsymbol{S}_N^{\mathrm{H}}(t)\boldsymbol{D}_N^{\mathrm{H}}\boldsymbol{D}_N\boldsymbol{S}_N(t), & \boldsymbol{S}_N^{\mathrm{H}}(t)\boldsymbol{D}_N^{\mathrm{H}}\boldsymbol{D}_r\boldsymbol{S}_N(t) \\ \boldsymbol{S}_N^{\mathrm{H}}(t)\boldsymbol{D}_r^{\mathrm{H}}\boldsymbol{D}_F\boldsymbol{S}_F(t), & \boldsymbol{S}_N^{\mathrm{H}}(t)\boldsymbol{D}_r^{\mathrm{H}}\boldsymbol{D}_N\boldsymbol{S}_N(t), & \boldsymbol{S}_N^{\mathrm{H}}(t)\boldsymbol{D}_r^{\mathrm{H}}\boldsymbol{D}_r\boldsymbol{S}_N(t) \end{bmatrix}\right\}, \tag{50}$$

$$\boldsymbol{D}_F=\left[\boldsymbol{d}_{F,-L}^{\mathrm{T}},\boldsymbol{d}_{F,-L+1}^{\mathrm{T}},\cdots,\boldsymbol{d}_{F,L}^{\mathrm{T}}\right]^{\mathrm{T}}, \tag{51}$$

$$\boldsymbol{D}_r=\left[\boldsymbol{d}_{r,-L}^{\mathrm{T}},\boldsymbol{d}_{r,-L+1}^{\mathrm{T}},\cdots,\boldsymbol{d}_{r,L}^{\mathrm{T}}\right]^{\mathrm{T}}, \tag{52}$$

$$\boldsymbol{D}_N=\left[\boldsymbol{d}_{N,-L}^{\mathrm{T}},\boldsymbol{d}_{N,-L+1}^{\mathrm{T}},\cdots,\boldsymbol{d}_{N,L}^{\mathrm{T}}\right]^{\mathrm{T}}. \tag{53}$$

Since the interested parameters are $\boldsymbol{\xi}_1=[\boldsymbol{\theta}_F^{\mathrm{T}},\boldsymbol{\theta}_N^{\mathrm{T}},\boldsymbol{r}^{\mathrm{T}}]^{\mathrm{T}}$, CRB can be obtained by the block matrix inversion formula as follows:

$$\mathrm{CRB}^{-1}(\boldsymbol{\xi}_1)=\boldsymbol{\Gamma}-\sum_{t=1}^{T}\mathrm{Re}\left\{\boldsymbol{\varepsilon}^{\mathrm{H}}(t)\boldsymbol{M}^{-1}\boldsymbol{\varepsilon}(t)\right\}. \tag{54}$$

In order to get the closed-form expression for CRB, CRB can be divided into four parts in the same way of [17]:

$$\mathrm{CRB}^{-1}(\boldsymbol{\xi}_1)=I_cT\begin{bmatrix} \mathrm{CRB}_1^{-1}(\boldsymbol{\xi}_1) & \mathrm{CRB}_2^{-1}(\boldsymbol{\xi}_1) \\ \mathrm{CRB}_3^{-1}(\boldsymbol{\xi}_1) & \mathrm{CRB}_4^{-1}(\boldsymbol{\xi}_1) \end{bmatrix} \tag{55}$$

where

$$\mathrm{CRB}_1^{-1}(\boldsymbol{\xi}_1)=\mathrm{Re}\left\{\left(\boldsymbol{D}_F^{\mathrm{H}}\boldsymbol{P}_A\boldsymbol{D}_F\right)\odot\boldsymbol{Q}_1^{\mathrm{T}}\right\}, \tag{56}$$

$$\mathrm{CRB}_2^{-1}(\boldsymbol{\xi}_1)=\mathrm{Re}\left\{\left[\boldsymbol{D}_F^{\mathrm{H}}\boldsymbol{P}_A\boldsymbol{D}_N,\boldsymbol{D}_F^{\mathrm{H}}\boldsymbol{P}_A\boldsymbol{D}_r\right]\odot\left[\boldsymbol{Q}_3^{\mathrm{T}},\boldsymbol{Q}_3^{\mathrm{T}}\right]\right\}, \tag{57}$$

$$\mathrm{CRB}_3^{-1}(\boldsymbol{\xi}_1)=\mathrm{Re}\left\{\begin{bmatrix} \boldsymbol{D}_N^{\mathrm{H}}\boldsymbol{P}_A\boldsymbol{D}_F \\ \boldsymbol{D}_r^{\mathrm{H}}\boldsymbol{P}_A\boldsymbol{D}_F \end{bmatrix}\odot\begin{bmatrix} \boldsymbol{Q}_2^{\mathrm{T}} \\ \boldsymbol{Q}_2^{\mathrm{T}} \end{bmatrix}\right\}, \tag{58}$$

$$\mathrm{CRB}_4^{-1}(\boldsymbol{\xi}_1)=\mathrm{Re}\left\{\begin{bmatrix} \boldsymbol{D}_N^{\mathrm{H}}\boldsymbol{P}_A\boldsymbol{D}_N & \boldsymbol{D}_N^{\mathrm{H}}\boldsymbol{P}_A\boldsymbol{D}_r \\ \boldsymbol{D}_r^{\mathrm{H}}\boldsymbol{P}_A\boldsymbol{D}_N & \boldsymbol{D}_r^{\mathrm{H}}\boldsymbol{P}_A\boldsymbol{D}_r \end{bmatrix}\odot\begin{bmatrix} \boldsymbol{Q}_4^{\mathrm{T}} & \boldsymbol{Q}_4^{\mathrm{T}} \\ \boldsymbol{Q}_4^{\mathrm{T}} & \boldsymbol{Q}_4^{\mathrm{T}} \end{bmatrix}\right\}, \tag{59}$$

where "$\odot$" represents the Hadamard-Schur matrix product, and $\boldsymbol{P}_A=\boldsymbol{I}-\boldsymbol{A}\boldsymbol{A}^{\perp}$. When all sources are FFSs, the $\mathrm{CRB}^{-1}(\boldsymbol{\xi}_1)$ is simplified to $\mathrm{CRB}_1^{-1}(\boldsymbol{\xi}_1)$. When all sources are NFSs, $\mathrm{CRB}^{-1}(\boldsymbol{\xi}_1)$ can be simplified to $\mathrm{CRB}_4^{-1}(\boldsymbol{\xi}_1)$.

Since the closed-form expression for the PDF of SαS distribution exists only when $\alpha=1$ and $\alpha=2$, the PDF of SαS distribution can be approximated by the Cauchy-Gaussian mixture (CGM) model [31]. The bi-parameter CGM model is a representative model with low computational complexity, it can be expressed as

$$f(u)=(1-\chi)\exp\frac{-u^2}{4\gamma^2}\left(2\gamma\sqrt{\pi}\right)^{-1}+\chi\gamma\left(\pi\left(u^2+\gamma^2\right)\right)^{-1} \tag{60}$$

where $\chi=2-\alpha$ is the mixture ratio, and $\gamma(\gamma>0)$ is the dispersion parameter. I_c can be calculated from (43) and (60). Finally, the CRB for the mixed sources under impulsive noise can be obtained.

5. Simulation results

There are several existing localization methods for mixed NFSs and FFSs used for comparison. The MBODS method [17] has great performance under Gaussian noise, and FLOC can suppress impulsive noise. Therefore, the FLOC and MBODS are combined to obtain FLOC-MBODS. Taking FLOC-MBODS, SP-GESPRIT [13], M-MUSIC [18] and CRB as comparison to prove the performance of the proposed method.

In all experiments, the number of elements in ULA is 9, and the spacing $d=\lambda/4$, simulation results are obtained from the mean of 500 independent Monte Carlo trials, and $N_e=500$. For the methods mentioned in the experiment, the search interval is selected as 0.1. The value of the fractional factor for SP-GESPRIT and FLOC-MBODS are set as 0.5. If the experiments do not specify the locations of sources, there are one FFS which is located in $(\theta_1=25^\circ)$ and one NFS which is located in $(\theta_2=8^\circ,r_2=2\lambda)$. Both FFS and NFS are deterministic unknown sequence with equal power. The generalized signal to noise ratio (GSNR) is defined as

$$\mathrm{GSNR}=10\lg\left(\mathrm{E}\left\{\boldsymbol{s}(t)\boldsymbol{s}^{\mathrm{H}}(t)\right\}\cdot\gamma^{-1}\right). \tag{61}$$

The parameter estimation results take root mean square error (RMSE) and probability of successful estimation (PSE) as standard. RMSE is defined as

$$\mathrm{RMSE}(\zeta)=\sqrt{\sum_{\hat{n}=1}^{N_e}\left(\zeta-\hat{\zeta}_{\hat{n}}\right)^2\cdot N_e^{-1}} \tag{62}$$

where ζ is the actual value of parameter, $\hat{\zeta}_{\hat{n}}$ is the estimated value of parameter in the $\hat{n}$th Monte Carlo repetition experiment, and N_e represents the number of independent Monte Carlo trials. PSE is defined as

$$\mathrm{PSE}=\frac{\tilde{N}_e}{N_e} \tag{63}$$

where $\tilde{N}_e$ is the number of successes. When $\left|\zeta-\hat{\zeta}_{\hat{n}}\right|\leqslant 1$, $\tilde{N}_e=\tilde{N}_e+1$.

5.1 Experiment 1

The first simulation experiment demonstrates the influence of the weighting factors p_1 and p_2. Due to $p_1+p_2=1$, three different values of p_1 are selected to verify the optimal range of p_1.

Table 1 shows the RMSE of DOAs and ranges for two sources when GSNR = 10 dB, the number of snapshots is $T=200$, characteristic exponent α increments are from 0.8 to 2, threshold value $p_3=5.1$. In Table 1, when $\alpha<1$, the impulse of background noise is strong, the proposed method can achieve better anti-impulsive effect with $p_1=0.2$. However, as α increases, the performance when $p_1=0.8$ is better than the performance when $p_1=0.2$ and $p_1=0.5$. Therefore, it can be concluded that the optimal p_1 is related to the working environment. Under strong impulse noise, a smaller value of p_1 can achieve better performance. On the contrary, when the impulse of background noise is weak, the value of p_1 needs to be larger to achieve better performance.

Table 1 Localization results versus α

Parameter	p_1	Characteristic exponent α							
		0.800 0	0.971 4	1.142 9	1.314 3	1.485 7	1.657 1	1.828 6	2.000 0
RMSE of DOAs/ (°)	0.2	2.843 4	0.692 0	0.536 3	0.424 6	0.353 5	0.298 1	0.247 9	0.220 6
	0.5	2.969 7	0.693 1	0.536 2	0.422 3	0.347 5	0.296 7	0.246 9	0.220 5
	0.8	3.100 7	0.697 3	0.530 5	0.417 3	0.353 3	0.290 6	0.242 7	0.218 5
RMSE of ranges/m	0.2	0.998 3	0.423 4	0.306 1	0.246 2	0.218 4	0.190 9	0.170 6	0.159 4
	0.5	0.968 4	0.430 9	0.308 0	0.245 8	0.216 5	0.189 9	0.167 9	0.156 7
	0.8	1.224 6	0.438 5	0.305 7	0.245 7	0.214 9	0.189 2	0.163 9	0.153 6

According to the conclusion drawn from Table 1, in order to further determine the optimal range of p_1, Table 2 shows the RMSE of the DOAs and ranges when characteristic exponent is $\alpha=1.5$, GSNR increments are from 0 dB to 20 dB, the rest of experimental conditions remain unchanged. In Table 2, it can be clearly observed that when $p_1=0.8$, the RMSE of DOAs and ranges are both smaller. Above all, it can be concluded that the value of p_1 does not cause the performance of the proposed method to deteriorate but will affect the localization accuracy to a certain extent. The optimal value of p_1 is affected by factors such as characteristic exponent α. Combining Table 1 and Table 2, it can be seen that the value of p_1 which is between $[0.75, 0.9]$ can ensure robust and accurate localization under various background noises.

Table 2 Localization results versus GSNR under α=1.5

Parameter	p_1	GSNR/dB							
		0.000 0	2.857 1	5.714 3	8.571 4	11.426 8	14.285 7	17.142 9	20.000 0
RMSE of DOAs/ (°)	0.2	1.172 6	0.732 6	0.473 4	0.322 5	0.241 2	0.175 2	0.132 7	0.110 3
	0.5	1.160 0	0.729 2	0.466 2	0.317 2	0.240 2	0.174 7	0.133 2	0.106 3
	0.8	1.155 4	0.726 0	0.462 1	0.316 6	0.235 7	0.173 2	0.131 6	0.102 5
RMSE of ranges/m	0.2	0.943 7	0.569 0	0.404 0	0.291 6	0.210 3	0.183 7	0.146 8	0.121 7
	0.5	0.934 0	0.568 1	0.401 9	0.291 5	0.211 2	0.178 6	0.145 8	0.116 0
	0.8	0.932 2	0.564 0	0.400 7	0.291 2	0.206 8	0.177 6	0.142 1	0.111 4

5.2 Experiment 2

In the second simulation experiment, characteristic exponent is $\alpha=1.5$, the number of snapshots is $T=200$, GSNR increments are from 0 dB to 25 dB, the weighting factors $p_1=0.87$ and $p_2=0.13$, and the threshold value $p_3=5.1$. The RMSE of FLOC-MBODS, SP-GESPRIT, M-MUSIC, and CRB are also plotted for comparison.

As seen from Fig. 2, the proposed method has smaller RMSE than the other methods and is closer to CRB. When $\alpha=1.5$, $T=200$, GSNR = 25 dB, the RMSE of θ_1, θ_2, and r_2 are 0.084 1, 0.089 2, and 0.105 3 respectively, and the CRB are 0.023 4, 0.022 1, 0.032 0, respectively.

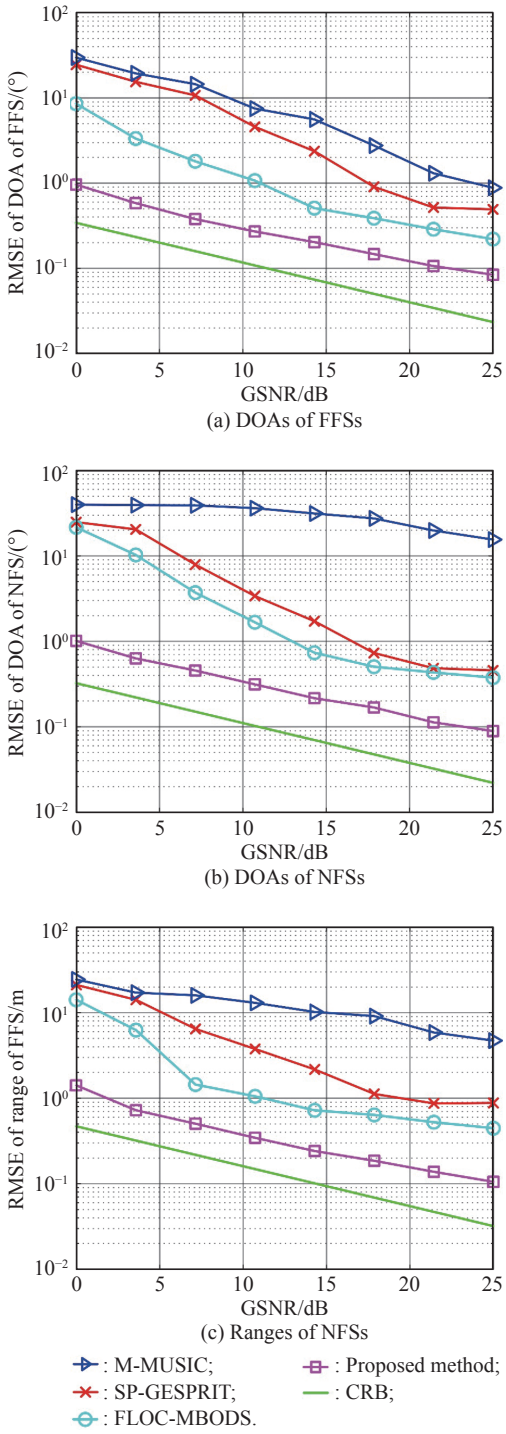

Fig. 2 RMSE versus GSNR

Corresponding to this, Fig. 3 shows the PSE of θ_1, θ_2, and r_2 versus GSNR. In Fig. 3, the conclusion similar to Fig. 2 can be obtained too. The PSE of the proposed method can still reach 70% at GSNR = 0 dB, which is higher than the comparison methods. With the increase of GSNR, the PSE gradually increases and reaches 100%. The proposed method can still have a high PSE when the GSNR is low. The PSE curve of the TSMUSIC method proves that the existing mixed source localization methods fail seriously under impulsive noise environment without additional anti-impulsive operation. Therefore, the proposed method has certain engineering practical value.

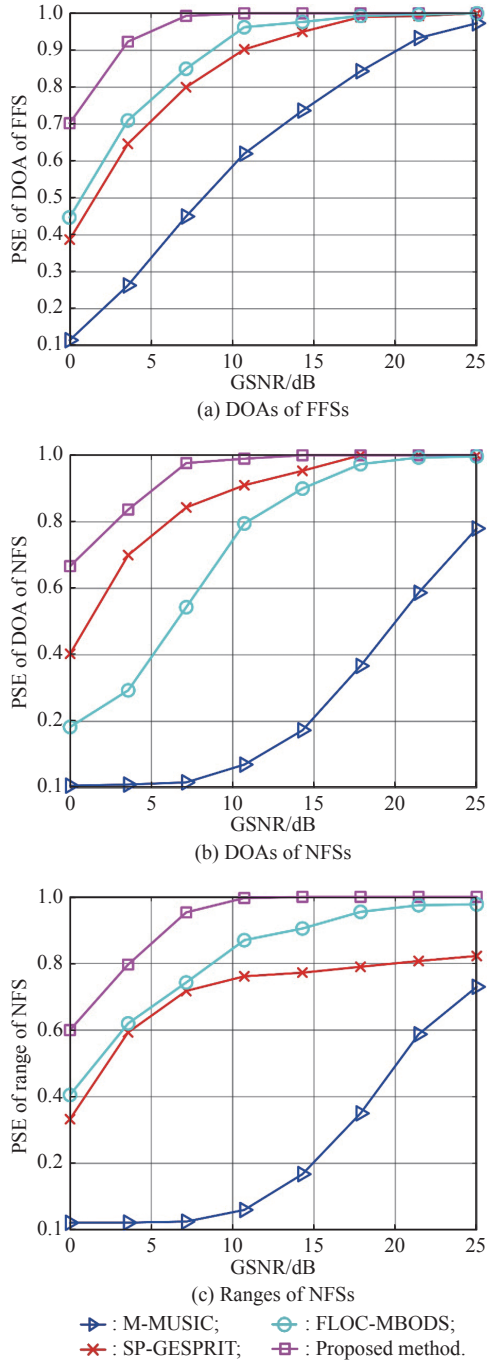

Fig. 3 PSE versus GSNR

When the locations of sources change, the location of FFS is ($\theta_1 = 33°$), the location of NFS is ($\theta_2 = -8°$, $r_2 = 2.5\lambda$), the number of snapshots is $T = 500$, the characteristic exponent is $\alpha = 1.5$, and the rest conditions remain unchanged. This experiment demonstrates the performance of the proposed method under different locations.

As seen from Fig. 4 and Fig. 5, the proposed method has smaller RMSE than the other methods. Compared with Fig. 2 and Fig. 3, the performance of the proposed method has been improved due to the increase in the number of snapshots and the change of locations. The SP-GESPRIT method estimates the DOAs of NFSs and FFSs simultaneously through the GESPRIT algorithm, but the accuracy of the SP-GESPRIT method is low.

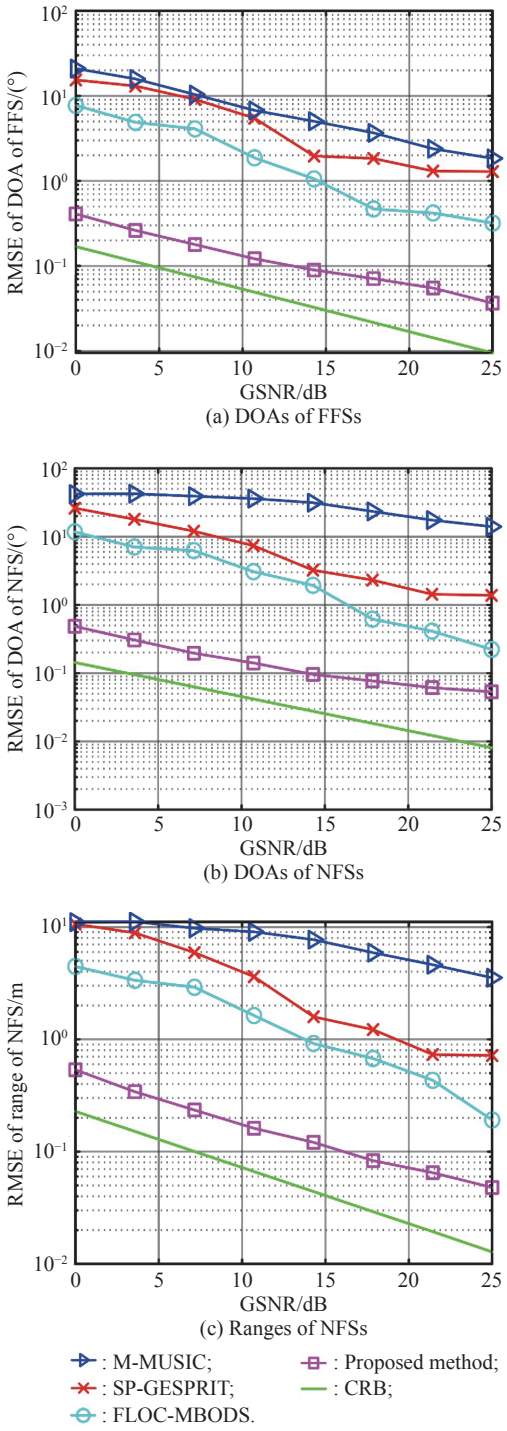

Fig. 4 RMSE versus GSNR under different locations

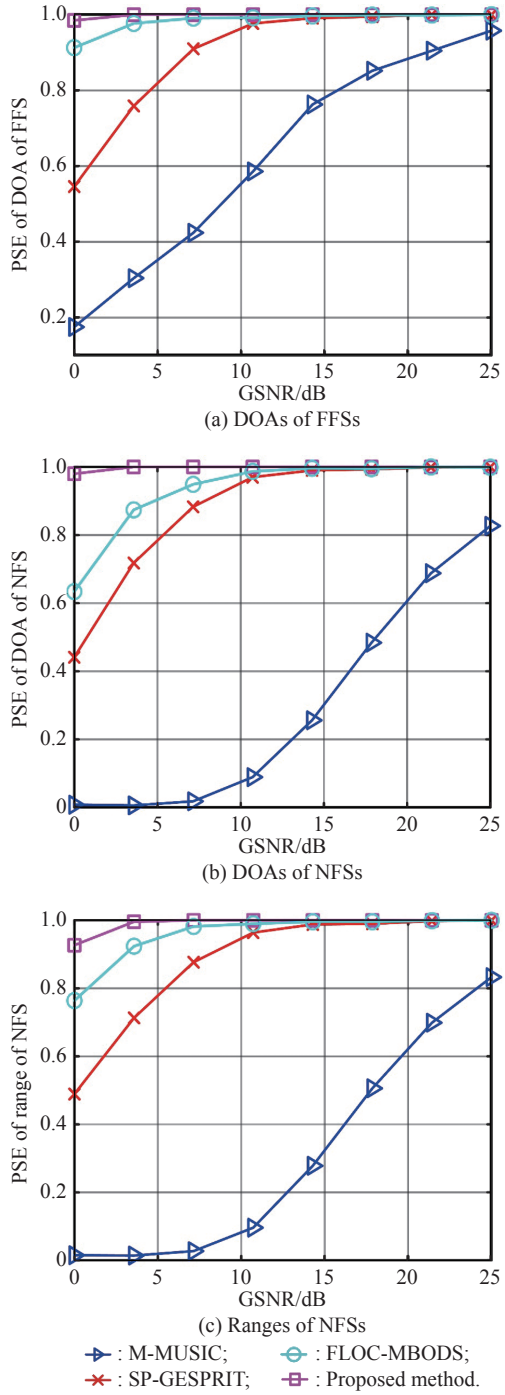

Fig. 5 PSE versus GSNR under different locations

5.3 Experiment 3

GSNR is set as 10 dB, the number of snapshots T increases from 250 to 1 100, and the rest conditions are the same as the second simulation experiment. This experiment evaluates the influence of T.

In Fig. 6, the RMSE of the proposed method is less than the other three comparison methods. As the number of snapshots decreases, the proposed method can still have a smaller RMSE. Due to the loss of array aperture in

the FLOC-MBODS method, the performance of the FLOC-MBODS method is limited when estimating the DOAs and ranges of NFSs, and RMSE tends to stabilize when $T \geqslant 600$. To sum up, the proposed method still has performance advantages when the number of snapshots changes and can perform more robust and accurate positioning under impulsive noise environment.

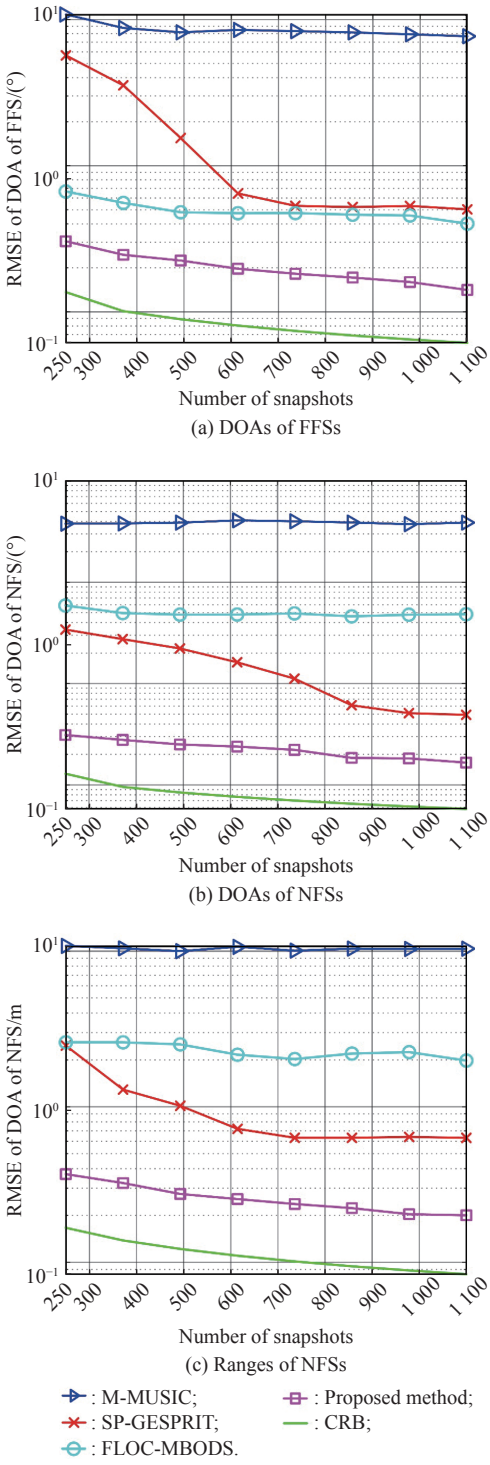

Fig. 6 RMSE versus number of snapshots

In Fig. 7, when $T = 250$, the PSE of the proposed method reaches 0.998, 0.998, and 0.990 respectively, and the proposed method can localize sources successfully. Compared with other methods, the PSE of the proposed method is higher. Combining Fig. 6 and Fig. 7, it is proven that the proposed method has higher localization accuracy and requires less snapshots.

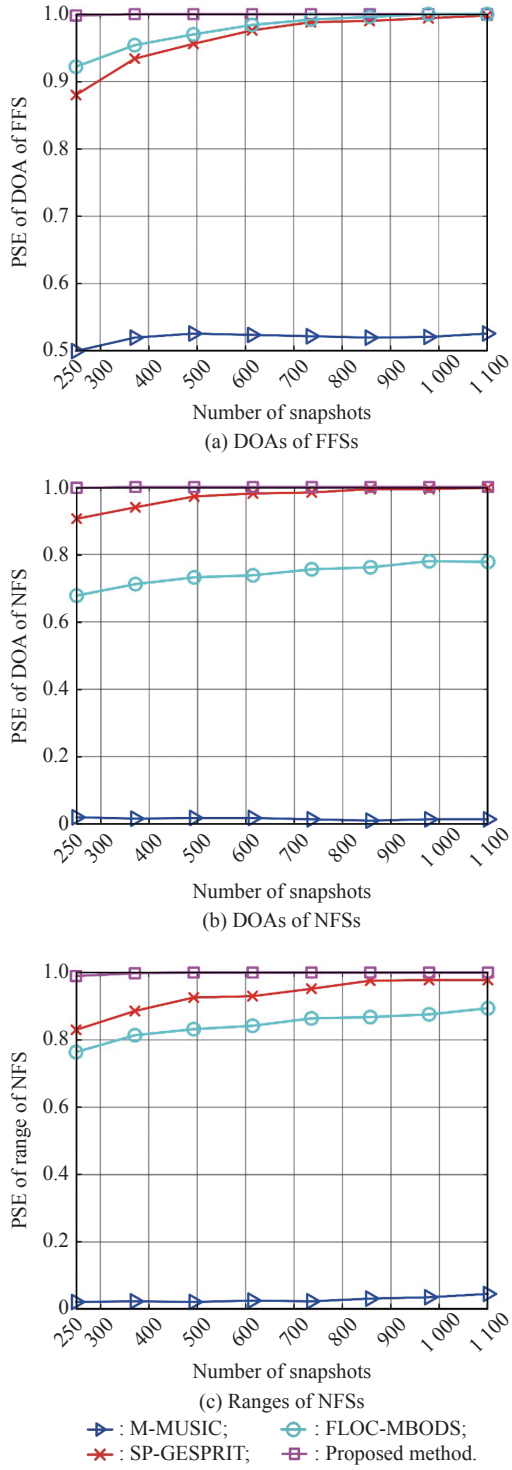

Fig. 7 PSE versus number of snapshots

5.4 Experiment 4

In this simulation experiment, the number of snapshots is $T = 300$, GSNR = 8 dB, and characteristic exponent α increases from 0.8 to 2.

In Fig. 8, the PSE of the proposed method is superior to that of other comparison methods under both impulsive noise ($\alpha < 2$) and Gausses noise ($\alpha = 2$). When $\alpha = 0.8$, the PSE of the parameters estimated by the proposed algorithm are 0.912, 0.870, and 0.866 respectively. The above data demonstrate that the proposed method can also perform robust localization when $\alpha < 1$. On the contrary, the performance of the SP-GESPRIT method and the FLOC-MBODS method deteriorates seriously, which indicates that the FLOC cannot resist impulsive noise effectively. When $\alpha = 2$, the background noise follows Gaussian distribution. The M-MUSIC method can also achieve great localizing performance, and the PSE of it can reach 100%. The proposed method can adapt to the noise environment with different characteristic exponents.

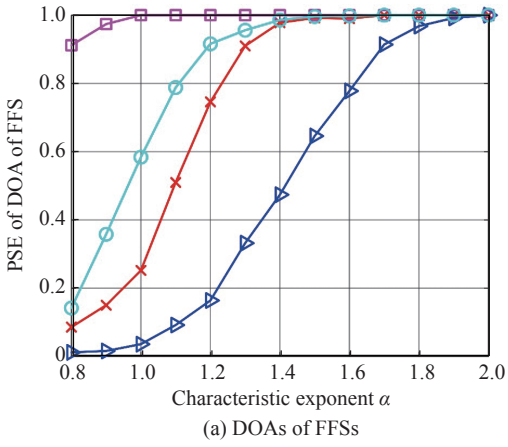

(a) DOAs of FFSs

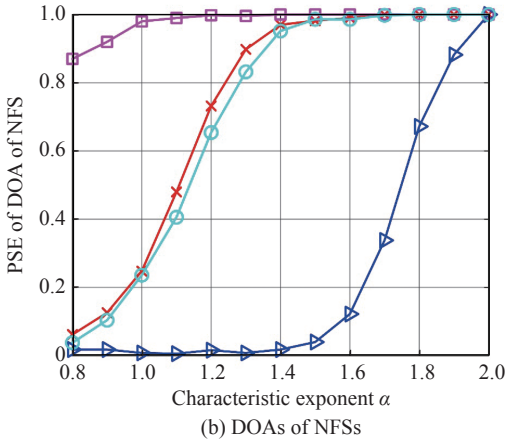

(b) DOAs of NFSs

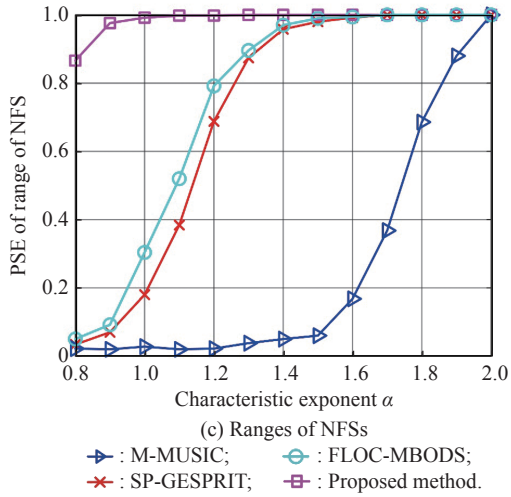

(c) Ranges of NFSs

Fig. 8 PSE versus characteristic exponent α

5.5 Experiment 5

This experiment demonstrates the performance of the proposed method under Gaussian noise and compares the simulation time of all four methods. There are one FFS located in ($\theta_1 = 25.5°$) and one NFS located in ($\theta_2 = 25°$, $r_2 = 3.5\lambda$). The number of snapshots is $T = 500$, characteristic exponent is $\alpha = 2$, and GSNR increases from 0 dB to 25 dB. Background noise follows Gaussian distribution, the value of the fractional factor for the SP-GESPRIT method and the FLOC-MBODS method are set as 1 and the threshold value p_3 of the proposed method is ∞, that is, no anti-impulsive noise operation is performed.

In Fig. 9 and Fig. 10, when the DOAs of FFS is close to the DOA of NFS, the performance of the SP-GESPRIT method will fail seriously, because the number of spectral peaks is less than the number of sources. The SP-GESPRIT method fails in this situation, and the RMSE of the SP-GESPRIT method does not improve much with the increase of GSNR. In Fig. 10(a) and Fig. 10(b), since the judgment criterion for successful estimation is that the difference between the estimated DOAs and the real DOAs is not more than 1°, and $\theta_1 - \theta_2 = 0.5°$, the PSE of DOAs increases with the increase of GSNR, but the RMSE remains large.

Combining Fig. 2(a) and Fig. 9(a), the performance of the proposed method is the same as that of the MBDOS method and the TSMUSIC method when estimating the DOAs of FFSs under Gaussian distribution noise. However, under impulsive noise environment, the performance of the proposed method is better than the performance of FLOC-MBODS method. It can be concluded that compared with the the FLOC, the proposed weighted outlier filter can better suppress the background impulsive noise and improve the positioning accuracy.

Compared with the M-MUSIC method and the MBODS

method, when estimating the parameters of NFS, the proposed method can reasonably separate FFSs and NFSs and there is no array aperture loss. Therefore, the estimation accuracy of NFSs is higher than the M-MUSIC method and the MBODS method. Therefore, it can be concluded that compared with the existing methods, the performance of the proposed method still has a smaller RMSE and a higher PSE in Gaussian noise environment.

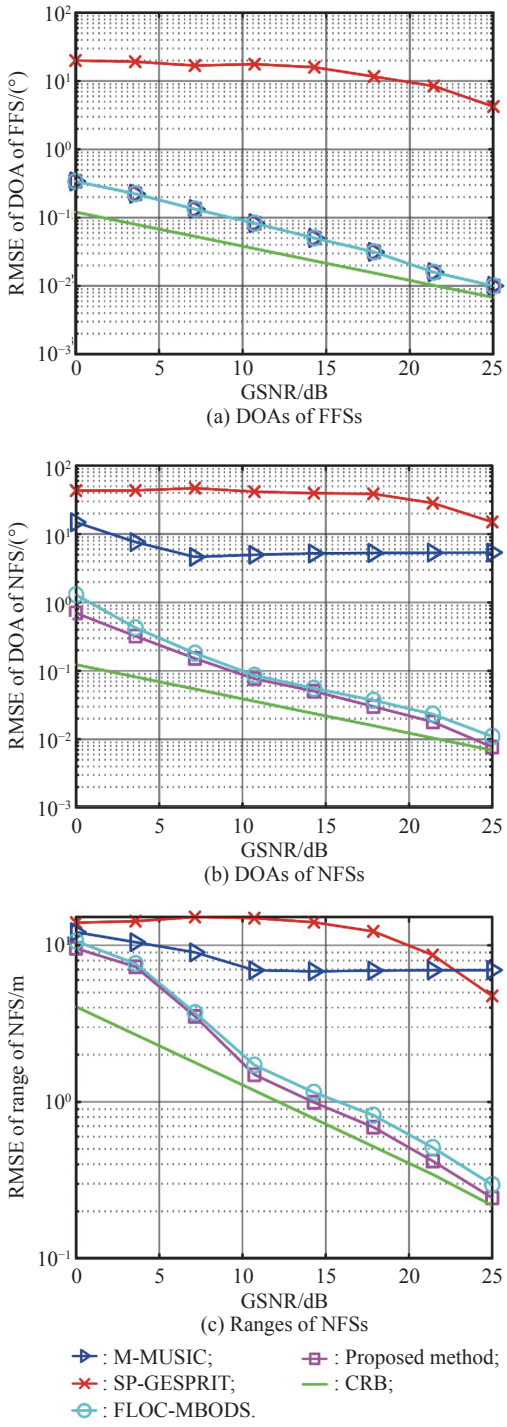

Fig. 9 RMSE versus GSNR under Gaussian noise

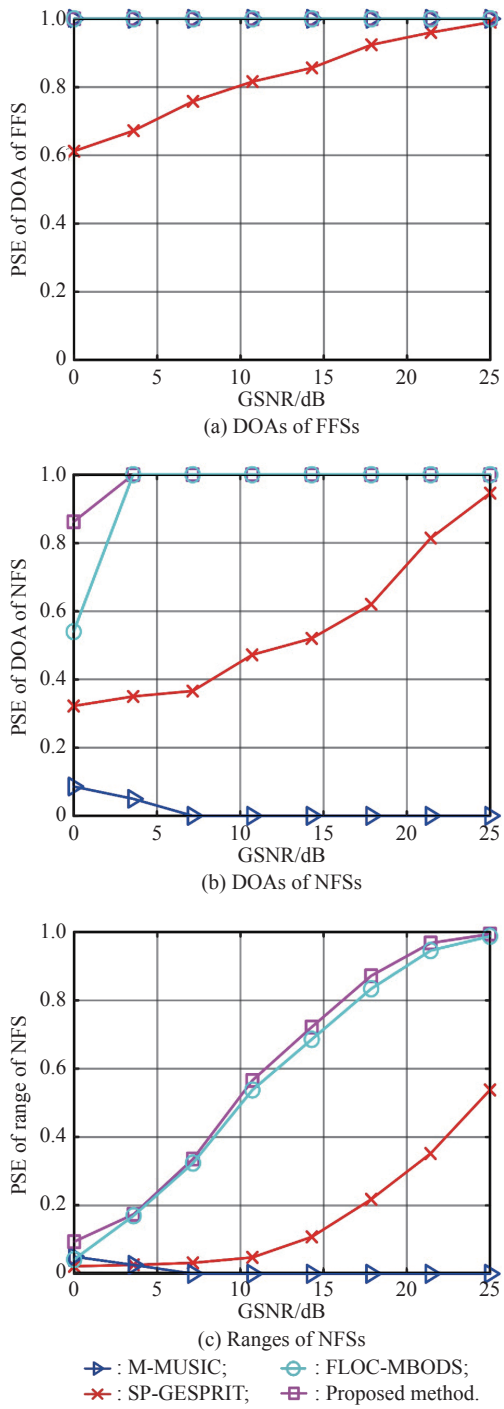

Fig. 10 RMSE versus GSNR under Gaussian noise

In Table 3, the simulation time of each method is given. It can be concluded that the computational complexity of the proposed method is relatively small, only higher than that of the SP-GESPRIT method. Compared with the M-MUSIC method and the MBODS method, the proposed method improves the estimation accuracy and reduces the computational complexity.

Table 3 Time of simulation s

Method	Simulation time
MBODS	11.126 7
SP-GESPRIT	3.763 0
M-MUSIC	21.017 9
The proposed	9.568 9

6. Conclusions

In this paper, for the case where NFSs and FFSs exist simultaneously under impulsive noise, a robust localization method is proposed. The weighted outlier filter is developed to resist the influence of impulsive noise. When estimating the locations of NFSs, the proposed method takes advantage of the decomposability of steering vector, which reduces computational complexity relatively while ensuring positioning accuracy. Since the proposed method can realize the separation of mixed sources, it is also suitable for pure FFSs or NFSs localization without redundant computation. The CRB which provides a theoretical minimum bound for scholars to further study the localization method for the mixed sources under impulsive noise is derived too. The simulation results of experiments which use PSE and RMSE as evaluation indicators prove the superiority of the proposed method under background noise with different GSNRs, the number of snapshots, and the characteristic exponent. There are still some problems to be solved. For example, due to the existence of multipath transmission in practical applications, the sources may not conform to the assumption of mutual independence. In this situation, the subspace-based algorithm cannot be used directly. Further research is needed on the localization of mixed sources which are coherent.

References

[1] KRIM H, VIBERG M. Two decades of array signal processing research: the parametric approach. IEEE Signal Processing Magazine, 1996, 13(4): 67–94.

[2] NING Y M, MA S, MENG F Y, et al. DOA estimation based on ESPRIT algorithm method for frequency scanning LWA. IEEE Communications Letters, 2020, 24(7): 1441–1445.

[3] LI P, LI J F, ZHANG Q T, et al. A DOA estimation method for UCA based on orthogonal subspace compensation. IEEE Communications Letters, 2021, 25(11): 3561–3564.

[4] CAI R Y, TIAN Q, QIU T S. A low complexity DOA estimation method of CD sources in impulsive noise. IEEE Access, 2021, 9: 142857–142868.

[5] VIKAS B, VAKULA D. Performance comparison of MUSIC and ESPRIT algorithms in presence of coherent signals for DOA estimation. Proc. of the International Conference of Electronics, Communication and Aerospace Technology, 2017: 403–405.

[6] WU X H, ZHU W P. Single far-field or near-field source localization with sparse or uniform cross array. IEEE Trans. on Vehicular Technology, 2020, 69(8): 9135–9139.

[7] LI W L, LIAO W J, FANNJIANG A. Super-resolution limit of the ESPRIT algorithm. IEEE Trans. on Information Theory, 2020, 66(7): 4593–4608.

[8] ZHANG W, HAN Y, JIN M, et al. An improved ESPRIT-like algorithm for coherent signals DOA estimation. IEEE Communications Letters, 2020, 24(2): 339–343.

[9] LEE S H, RYU C S, LEE K K. Near-field source localization using bottom-mounted linear sensor array in multipath environment. IEE Proceedings-Radar, Sonar and Navigation, 2002, 149(4): 202–206.

[10] PAN J J, SINGH PARTH R, MEN S Y. A search-free near-field source localization method with exact signal model. Journal of Systems Engineering and Electronics, 2021, 32(4): 756–763.

[11] HUANG Y D, BARKAT M. Near-field multiple source localization by passive sensor array. IEEE Trans. on Antennas and Propagation, 1991, 39(7): 968–975.

[12] LI S, LIN B, LI B, et al. 2-D parameter estimation of near field source based on robust propagator method. IEEE Journal of Radio Frequency Identification, 2019, 3(3): 157–163.

[13] QIU T S, WANG P. A novel method for near-field source localization in impulsive noise environments. Circuits, Systems and Signal Processing, 2016, 35: 4030–4059.

[14] CHEN G H, ZENG X P, JIAO S, et al. High accuracy near-field localization algorithm at low SNR using fourth-order cumulant. IEEE Communications Letters, 2020, 24(3): 553–557.

[15] LIANG J L, LIU D. Passive localization of mixed near-field and far-field sources using two-stage MUSIC algorithm. IEEE Trans. on Signal Processing, 2010, 58(1): 108–120.

[16] JIANG J J, DUAN F J, CHEN J. Three-dimensional localization algorithm for mixed near-field and far-field sources based on ESPRIT and MUSIC method. Progress in Electromagnetics Research, 2013, 136: 435–456.

[17] HE J, SWANY M N S, AHMAD M O. Efficient application of MUSIC algorithm under the coexistence of far-field and near-field sources. IEEE Trans. on Signal Processing, 2012, 60(4): 2066–2070.

[18] ZHENG Z, SUN J, WANG W Q, et al. Classification and localization of mixed near-field and far-field sources using mixed-order statistics. Signal Processing, 2018, 143: 134–139.

[19] DE FREITAS M L, EGAN M, CLAVIER L, et al. Capacity bounds for additive symmetric α-stable noise channels. IEEE Trans. on Information Theory, 2017, 63(8): 5115–5123.

[20] BRCICH R F, ISKANDER D R, ZOUBIR A M. The stability test for symmetric alpha-stable distributions. IEEE Trans. on Signal Processing, 2005, 53(3): 977–986.

[21] DONG X D, SUN M, ZHANG X F, et al. Fractional low-order moments based DOA estimation with co-prime array in presence of impulsive noise. IEEE Access, 2021, 9: 23537–23543.

[22] SONG A M. White noise array gain for minimum variance distortionless response beamforming with fractional lower order covariance. IEEE Access, 2018, 6: 71581–71591.

[23] LI S, HE R X, LIN B, et al. DOA estimation based on sparse representation of the fractional lower order statistics in impulsive noise. IEEE/CAA Journal of Automatica Sinica, 2018, 5(4): 860–868.

[24] HARI K V S, LALITHA V. Subspace-based DOA estimation using fractional lower order statistics. Proc. of the IEEE International Conference on Acoustics, Speech, and Signal

Processing, 2011: 2580–2583.
[25] LIU T H, MENDEL J M. A subspace-based direction finding algorithm using fractional lower order statistics. IEEE Trans. on Signal Processing, 2001, 49(8): 1605–1613.
[26] HU W M, LIU R F, LIN X M, et al. A deep learning method to estimate independent source number. Proc. of the 4th International Conference on Systems and Informatics, 2017: 1055–1059.
[27] ICHIGE K, HAMADA S, KASHIWAGI K, et al. Robust source number estimation based on denoising preprocessing. Proc. of the Sensor Signal Processing for Defence Conference, 2020. DOI: 10.1109/SSPD47486.2020.9272068.
[28] ZHANG J F, QIU T S. Stochastic Cramer-Rao bound for noncircular sources' DOA estimation in alpha-stable noise. Proc. of the IEEE 9th International Conference on Communication Software and Networks, 2017: 880–887.
[29] STOICA P, NEHORAI A. Performance study of conditional and unconditional direction-of-arrival estimation. IEEE Trans. on Acoustics, Speech, and Signal Processing, 1990, 38(10): 1783–1795.
[30] KOOCHAKZADEH A, PAL P. Cramer-Rao bounds for underdetermined source localization. IEEE Signal Processing Letters, 2016, 23(7): 919–923.
[31] LI X T, CHEN Z T, WANG S Y. An approximate representation of heavy-tailed noise: bi-parameter Cauchy-Gaussian mixture model. Proc. of the 9th International Conference on Signal Processing, 2008: 76–79.

Biographies

GAO Hongyuan was born in 1977. He received his M.S. and Ph.D. degrees in communication and information systems from Harbin Engineering University in 2005 and 2010, respectively. He is an associate professor in the College of Information and Communication Engineering at Harbin Engineering University. His current research interests include artificial intelligence, signal processing of array, and wireless communication system.
E-mail: gaohongyuan@hrbeu.edu.cn

ZHANG Yuze was born in 2000. He received his B.S. degree from Harbin Engineering University in 2021. He is studying towards his M.S. degree in the College of Information and Communication Engineering at Harbin Engineering University. His current research interests include signal processing and artificial intelligence.
E-mail: zhangyuze@hrbeu.edu.cn

DU Ya'nan was born in 1992. She received her M.S. degree in communication engineering from Harbin Engineering University in 2017. She is working towards her Ph.D. degree in the College of Information and Communication Engineering at Harbin Engineering University, China. Her current research interests include swarm intelligence and signal processing.
E-mail: wenhuamo@126.com

CHENG Jianhua was born in 1977. He received his M.S. and Ph.D. degrees in navigation, guidance, and control from Harbin Engineering University in 2006. He is a professor in the College of Control Science and Engineering at Harbin Engineering University. His current research interests include inertial navigation system, satellite navigation, and integrated navigation.
E-mail: chengjianhua@hrbeu.edu.cn

CHEN Menghan was born in 1994. She received her B.S. degree from Harbin Engineering University in 2016. She is a doctoral candidate of information and communication engineering in the College of Information and Communication Engineering at Harbin Engineering University, China. Her current research interests include intelligence computing and array signal processing.
E-mail: moqunjisuan@163.com